

Intrinsic plasma rotation and Reynolds stress at the plasma edge in the HSX stellarator

This content has been downloaded from IOPscience. Please scroll down to see the full text.

2016 Nucl. Fusion 56 036002

(<http://iopscience.iop.org/0029-5515/56/3/036002>)

View [the table of contents for this issue](#), or go to the [journal homepage](#) for more

Download details:

IP Address: 128.104.46.196

This content was downloaded on 10/03/2016 at 20:41

Please note that [terms and conditions apply](#).

Intrinsic plasma rotation and Reynolds stress at the plasma edge in the HSX stellarator

R.S. Wilcox^{1,2,a}, J.N. Talmadge², D.T. Anderson², F.S.B. Anderson² and J.D. Lore¹

¹ Oak Ridge National Laboratory, Oak Ridge, TN 37831, USA

² Department of Electrical and Computer Engineering, University of Wisconsin: Madison, Madison, WI 53706, USA

E-mail: wilcoxr@fusion.gat.com

Received 14 July 2015, revised 16 December 2015

Accepted for publication 29 December 2015

Published 5 February 2016



Abstract

Using multi-tipped Langmuir probes in the edge of the HSX stellarator, the radial electric field and parallel flows are found to deviate from the values calculated by the neoclassical transport code PENTA for the optimized quasi-helically symmetric (QHS) configuration. To understand whether Reynolds stress might explain the discrepancy, fluctuating floating potential measurements are made at two locations in the torus corresponding to the low field and high field sides of the device. The measurements at the two locations show clear evidence of a gradient in the Reynolds stress. However, the resulting flow due to the gradient in the stress is found to be large and in opposite directions for the two locations. This makes an estimation of the flux surface average using a small number of measurement locations impractical from an experimental perspective. These results neither confirm nor rule out whether Reynolds stress plays an important role for the QHS configuration. Measurements made in configurations with the quasi-symmetry degraded show even larger flows and greater deviations from the neoclassically calculated velocity profiles than the QHS configuration while the fluctuation magnitudes are reduced. Therefore, for these configurations in particular, the Reynolds stress is most likely not responsible for the additional momentum.

Keywords: quasi-symmetric stellarators, plasma rotation, Reynolds stress, Langmuir probes

(Some figures may appear in colour only in the online journal)

1. Introduction

Unlike a classical stellarator, which has multiple terms in its magnetic spectrum and therefore multiple classes of trapped particles which lead to non-ambipolar particle transport, the ambipolarity constraint is satisfied automatically (total charge flux $\sum_a q_a \Gamma_a(E_r) = 0$ for all values of E_r) for an ideal tokamak [1–3] or a perfectly quasi-symmetric stellarator [4, 5]. The radial electric field and intrinsic rotation in these configurations must therefore be determined using higher order gyrokinetic calculations [6–8].

All real devices have non-zero ripple, though, which for arbitrary values of radial electric field will lead to some finite amount of non-ambipolar neoclassical particle transport and radial current. This radial current drives the potential on each surface toward a neoclassical root solution of E_r at which the total particle transport has no net charge and the ambipolarity condition is met. In tokamaks approaching axisymmetry, however, the intrinsic rotation appears to be determined by factors other than the neoclassical transport caused by ripple [9], indicating that there is some finite amount of ripple that is acceptable while still allowing arbitrary rotation and radial electric field values to first order in the drift kinetic equation. If a magnetic configuration is approximately quasi-symmetric and the non-ambipolar neoclassical particle transport is

^a Present affiliation: Oak Ridge National Laboratory; Present address: General Atomics, San Diego, CA, USA.

reduced to a small enough value, then the turbulence-driven Reynolds stress (the exchange of momentum between fluid fluctuations and the mean fluid velocity) may provide enough torque to rotate the plasma and set E_r to a different value that still results in zero net radial current when all of the stresses are accounted for [5, 10, 11].

Previous experiments have explored the role of Reynolds stress in plasmas with an approximate direction of symmetry. In the cylindrical plasma device CSDX, mean azimuthal flow has been measured which is sustained against viscosity by the Reynolds stress [12, 13]. The azimuthal rotation calculated by balancing the Reynolds stress measured using Langmuir probes with the calculated ion-ion and ion-neutral viscosity was found to agree well with the rotation found by a time delay estimation technique using adjacent probe pins.

In experiments at the DIII-D tokamak, measurements of the Reynolds stress were made using Langmuir probes in the edge and compared against the intrinsic rotation in the toroidal direction as well. These measurements did not explain the intrinsic torque that must exist to drive the observed toroidal flows in H-mode plasmas, however [14, 15]. In this case, a kinetic model of thermal ion orbit loss accounted for approximately half of the inferred torque in the co-direction at the edge, and the remaining intrinsic toroidal rotation was unaccounted for. These experiments were performed in diverted H-mode plasmas with hot ions, which has significantly different edge physics than the HSX plasmas studied here, but it is nonetheless interesting to note that there is observed rotation that cannot be fully explained using measurements of the Reynolds stress in addition to existing models of intrinsic torque.

The HSX stellarator is the first stellarator optimized for quasi-symmetry, where the direction of symmetry has a helical $n = 4$, $m = 1$ mode structure [16]. Here n and m are the toroidal and poloidal mode numbers in Boozer coordinates, respectively [4]. In addition to the main coils that provide the magnetic field for the optimized quasi-helically symmetric magnetic configuration (QHS), HSX has a set of auxiliary coils that can be energized to intentionally break the designed optimization. The Mirror [17] and Flip-1-4 [18] configurations of the auxiliary coils are particular magnetic configurations that are designed to degrade the symmetry in the magnetic field strength while keeping other parameters, such as the rotational transform and plasma volume, close to their value in the QHS configuration. This allows a relatively direct comparison of confinement and transport properties with and without the quasi-symmetric optimization. The Mirror configuration mostly contributes a single large-amplitude $n = 4$, $m = 0$ mode, while the Flip-1-4 configuration contributes a smaller amplitude $n = 4$, $m = 0$ mode as well as an $n = 8$, $m = 0$ mode. Experiments presented here were performed in each of the three configurations, QHS, Mirror and Flip-1-4, as a scan of quasi-symmetric optimization, where the effective ripple ϵ_{eff} is used as a proxy for this optimization. Neoclassical transport in the low collisionality regime scales with $\epsilon_{\text{eff}}^{3/2}/\nu$, where ν is the particle collisionality [19]. Although the effective ripple is calculated to be as low as 2×10^{-3} in the core of the QHS configuration, in the edge region where probe

measurements are made here, it is approximately 1×10^{-2} in the QHS configuration, 2×10^{-2} in the Flip-1-4 configuration, and 8×10^{-2} in the Mirror configuration. For the data presented here in the outer radial regions of each configuration, thermal ions and electrons are in the plateau and low collisionality regimes, respectively.

It is important to note that the ripple in the edge of HSX, even in the optimized configuration, is an order of magnitude larger than NSTX with RMP coils. Turbulence has also been shown to increase with minor radius [20] and so the turbulence-free, perfectly quasi-symmetric model in neoclassical transport does not apply [5, 10]. Previous studies in HSX have shown that for the QHS configuration, thermal transport is dominated by anomalous rather than neoclassical effects throughout the plasma [18, 21]. Neoclassical transport is important in the core only when the quasisymmetry is degraded [18, 22]. More recently, measurements of plasma rotation and radial electric field have not agreed well with neoclassical modeling, particularly at the edge [23]. Part of the goal of this work was to help explain this discrepancy.

In this document, the competition of neoclassical non-ambipolar particle loss and momentum transport through the Reynolds stress will be explored by computational analysis and experiment. Section 2 introduces the Langmuir probes used in the experiment, section 3 presents the radial electric field and parallel flow measurements and compares these with neoclassical calculations for several magnetic configurations, the locally measured Reynolds stress in the QHS configuration is shown in section 4, and the contribution of Reynolds stress to the flows in the Flip-1-4 and Mirror configurations is analyzed in section 5. The paper concludes with a discussion of the results in section 6.

2. Reynolds stress probe design

Two sets of Langmuir probes were designed and installed to measure the radial electric field, parallel ion flow and local Reynolds stress profiles in HSX. Two pictures of the probe on the low-field side of the device are given in figure 1. The purpose of this specific probe configuration is to find the mean parallel flow velocity as well as the local fluctuating velocity components in each of the three orthogonal directions. Labels on the left picture indicate which pins are biased to measure the floating potential and ion saturation current, and labels on the right show the pairs of pins that are used to infer the three local velocity components. Tungsten is used as the conducting probe pin material and boron nitride is used as the insulating material.

Three of the pins of the probe are aligned perpendicular to the direction of the magnetic field lines, two of which are positioned on the same flux surface and a third that is recessed radially from the leading pins. By measuring the floating potential at each of these three locations, the instantaneous radial and bi-normal electric fields E_r and E_θ are extracted to infer the bi-normal and radial single-fluid plasma velocities v_θ and v_r , respectively. The bi-normal direction $\hat{\theta}$ (approximately ‘poloidal’) is defined here as the direction of positive $E_r \times B_0$ flow, so that

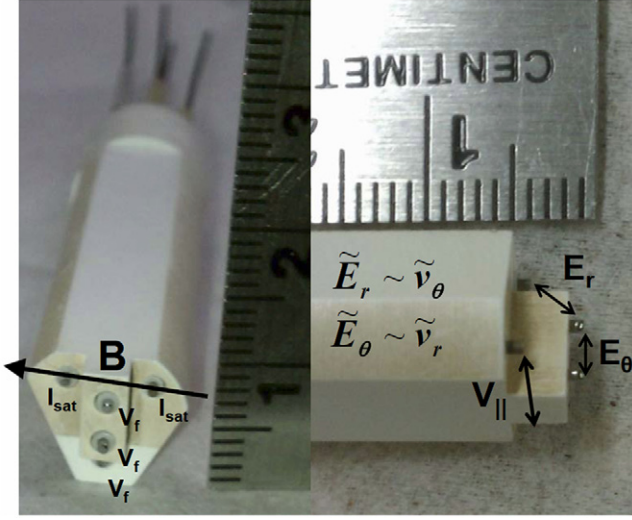


Figure 1. Pictures of the low-field side (LFS) Reynolds stress probe. Left: from the perspective of the plasma with \vec{B} from right to left, with pins labeled according to which signal it is biased to measure. Right: profile view, with \vec{B} going approximately into the page. The velocity components for which each of the pin signals are used to infer are labeled.

$$\tilde{v}_\theta = \frac{\tilde{\vec{E}} \times \vec{B}_0}{|B_0|^2} \cdot \hat{\theta} \approx \frac{\tilde{V}_{f12} - \tilde{V}_{f13}}{|B_0|}, \quad (1)$$

$$\tilde{v}_r = -\frac{\tilde{\vec{E}} \times \vec{B}_0}{|B_0|^2} \cdot \hat{r} \approx -\frac{\tilde{V}_{f12} - \tilde{V}_{f11}}{|B_0|}, \quad (2)$$

where the floating potential signals $V_{f11} \rightarrow V_{f13}$ are taken from the pins ordered 1 \rightarrow 3 from top to bottom in the center vertical row of the probe on the left in figure 1. Here \tilde{v} and \tilde{V}_{f1} denote the fluctuating components of local single-fluid $\vec{E} \times \vec{B}$ velocity and measured floating potential in time, respectively, on the timescale of a few turbulence decorrelation times or less ($\tau_d \approx 10 \mu\text{s}$ in these experiments). It is assumed that the fluctuations are purely electrostatic, which should be valid in these low β HSX plasmas [20] ($\beta < 10^{-4}$ where probe measurements are made). This formulation for the fluctuating quantities accounts for any mean T_e gradients that may exist between the pins, as the \tilde{V}_{f1} quantities are mean-free, but it does not account for fluctuating components of T_e on the scale length of the probe tip separation. Electron temperature fluctuations have been shown to be significant in the quantitative interpretation of differential Langmuir probe V_{f1} signals as E_θ fluctuations [24]. Because there are no measurements available to quantify T_e fluctuations directly, this effect is neglected in this work in order to get an estimate of the fluctuating plasma potential $\tilde{\phi}$ from the floating potential measurements.

The separation distance between the floating potential pins was chosen to ensure that a negligible fraction of particle trajectories that are incident on one pin would have also been collected by another pin, while minimizing the size of the probe to reduce the perturbation to the plasma. The pins are aligned to avoid shadowing by the magnetic field and the poloidal separation between the pins is 3 mm center-to-center.

Each pin has a 0.75 mm diameter, so there are about 3 thermal ion gyroradii between the pins ($\rho_i \approx 0.7 \text{ mm}$ here). The Debye length is on the order of $\sim 50 \mu\text{m}$ in the edge, so the probe tip sheaths do not overlap.

Two additional pins are then configured as a mach probe to measure the ion saturation current on either side of an insulating barrier, and are aligned on a field line to infer the parallel ion flow velocity. The mach probe collection areas are calibrated by taking repeated measurements first in the standard orientation and again with the probe orientation rotated by 180 degrees so that the pin locations are approximately flipped. The measurement given by the probe is the parallel mach number $M_\parallel = V_\parallel / (Kc_s)$, where $c_s = \sqrt{(T_e + T_i)/m_i}$ is the ion sound speed and K is a constant determined by the model. This is translated to a parallel velocity by assuming hydrogen ions and using the same T_e and T_i profiles that are given as inputs to the neoclassical calculations, as described later in section 3. An unmagnetized model by Hutchinson has been used to determine the value of $K = 1.34$ for this work [25].

Signals from the probes are sampled at 2.5 MHz using high-impedance digitizers connected to the sense resistor for each signal by a 50 Ohm coaxial cable with no analog amplification or filtering. A digital filter is applied above 300 kHz to reduce the noise from, for example, radio signals above 1 MHz. This does not produce any substantive changes to the results, except where noted for some analysis of fluctuating I_{sat} measurements.

2.1. Probe positioning and magnetic geometry

Two Reynolds stress probes are located in regions near the maximum of the variation of magnetic geometry on a flux surface. One probe is in a region of low field and ‘bad curvature’ ($\vec{\kappa} \cdot \nabla\psi > 0$, where curvature $\vec{\kappa} = (\hat{\mathbf{b}} \cdot \nabla)\hat{\mathbf{b}}$ with small flux expansion ($\nabla\psi > \langle \nabla\psi \rangle$), and the other is in a region of high field and ‘good curvature’ ($\vec{\kappa} \cdot \nabla\psi < 0$) with large flux expansion ($\nabla\psi < \langle \nabla\psi \rangle$). Due to the helical structure of the magnetic field strength in HSX, both the low-field side (LFS) and high-field side (HFS) probes are located on the outboard side of the device.

The cross section of the magnetic surfaces at each of the probe locations is given in figure 2 as calculated by vacuum field line following in the QHS configuration. The relative magnetic field strength is indicated by the color at each point, with red being the highest field strength ($\sim 1.1 \text{ T}$) and blue the lowest field strength ($\sim 0.9 \text{ T}$). Probe insertion points are plotted as arrows and accessible sampling points are plotted with black circles. The shaping of the magnetic surfaces does not change dramatically when the configuration is changed from QHS to Mirror or Flip-1-4. Based on calculations using the VMEC equilibrium solver [26], finite-beta effects are not expected to change the shaping of the surfaces significantly at the locations of the probes ($\beta < 10^{-4}$ here).

As seen in figure 2(a), the magnetic surfaces at the probe insertion point on the HFS port are not normal to the plane of the probe slide. The shape of the HFS probe is adjusted to account for this change in the angle of incidence compared to the picture of the LFS probe given in figure 1.

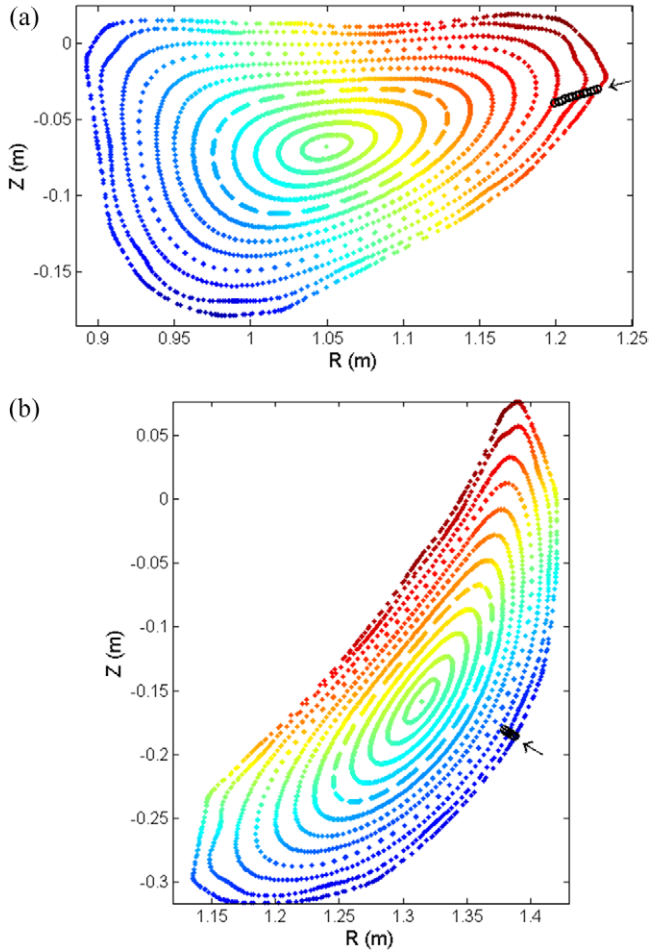


Figure 2. Magnetic surface cross sections at probe insertion locations on (a) the high-field side and (b) the low-field side probe locations in HSX, with colors indicating field strength at each surface point.

Although there are not expected to be large islands in the confinement region in HSX for these experiments, based on vacuum field line following, there is a small island chain where $\iota = 12/11$ near $r/a \approx 0.93$ which has a non-negligible width at the HFS probe location. Because of the oblique insertion angle, the island width is approximately 0.75 cm along the axis of the probe. The calculated island width at the LFS probe location is negligible (smaller than the probe pin size).

2.2. Magnetic geometry at probe locations

In order to investigate the variation of the Reynolds stress on a flux surface, the two probe locations were chosen to be located in regions near the extrema of magnetic field strength and normal curvature on a flux surface. Turbulence caused by microinstabilities is thought to be the source of the fluctuations which lead to the Reynolds stress in magnetized plasmas. For experimental parameters in HSX, trapped electron modes are calculated to be the most unstable modes and the dominant instability contributing to transport in the edge of the plasma [20, 21, 27].

The magnetic field strength normalized to the flux surface averaged value, $|B|/\langle B \rangle$, determines the local trapped particle

population which drives the trapped electron mode turbulence. This is plotted for the QHS configuration in figure 3(a) as a function of toroidal angle ϕ and poloidal angle θ in VMEC coordinates [26], where blue is low magnetic field strength relative to the flux surface average, and red is high magnetic field strength. The locations of the probes are indicated by white X's, with the LFS probe near $\phi \approx 1.3$ and the HFS probe located near $\phi \approx 4$. Both probes are located on the outboard side of the device, where the outboard midplane is $\theta = 0$.

The normal curvature for a magnetic surface at $r/a \approx 0.82$ in the QHS configuration is then plotted in figure 3(b), where blue is the largest 'bad' curvature and red is the largest 'good' curvature. The surface in both plots in figure 3 was traced using line following and the poloidal coordinates were determined by mapping the surface points onto the VMEC equilibrium. The Reynolds stress probe locations are indicated with black X's. As shown in figure 3, the LFS probe is in a region near the minimum of curvature on a flux surface (largest 'bad' curvature), while the HFS probe is in a region with only slightly higher than zero curvature (only slightly 'good' curvature).

The normal curvature at the probes does not change significantly between the QHS and Mirror configurations, however, the difference in magnetic field strength between the two probe locations is smaller in the Mirror configuration than it is in the QHS configuration. The field strength at all outboard ports (near $\theta = 0$) is similar in the Mirror configuration regardless of the toroidal angle due to the combination of the $n = 4, m = 1$ main field harmonic and the $n = 4, m = 0$ term which is added to break the symmetry. The modulation in field strength between the two probe locations in the Flip-1-4 configuration is larger than it is in Mirror but smaller than in QHS.

3. E_r and $V_{||}$ profiles and comparison to neoclassical calculations

For the experiments presented here, 44 kW of ECRH was injected into HSX plasmas with a magnetic field strength of 1 T on axis, and with interferometer-measured line-averaged densities of approximately $4 \times 10^{18} \text{ m}^{-3}$. Hydrogen gas puffing was used as the particle fueling, and boronization was used to condition the stainless steel walls. Probe data presented here was taken during the final 20 ms of each 50 ms discharge, when both macroscopic plasma parameters and probe measurements had reached a steady state.

3.1. Neoclassical modeling using PENTA

In order to compare the measured flows and radial electric field to what would be expected if neoclassical transport and damping were the dominant terms in the momentum balance, the PENTA code [28, 29] is used here to calculate the neoclassical ambipolar solution for E_r and $V_{||}$ based on experimental plasma parameters. Several terms are not calculated here which may be important to the particle transport, including ECRH-driven particle flux and ion orbit loss across the separatrix. Ion orbit loss is expected to be small, because

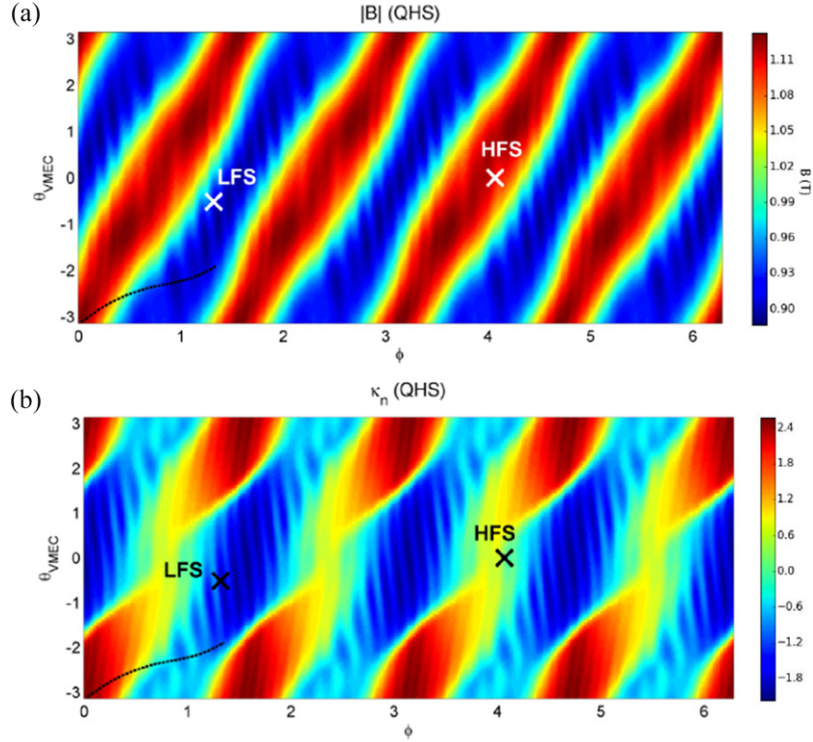


Figure 3. (a) Magnetic field strength and (b) normal curvature on a surface near $r/a \approx 0.82$ in the QHS configuration in VMEC coordinates. Probe locations are marked with X's and labeled LFS and HFS, and a representative field line is given as a dashed black line.

of a combination of high ion collisionality, long connection lengths to the wall just outside the last closed flux surface, and small ion banana orbit widths [30].

PENTA uses the neoclassical ambipolarity constraint $\sum_a q_a \Gamma_a(E_r) = 0$, where q_a is the charge of species a and $\Gamma_a(E_r)$ is the calculated neoclassical particle flux for species a as a function of radial electric field. First a fixed-boundary vacuum equilibrium is calculated using the VMEC equilibrium solver [26]. The use of a vacuum equilibrium is justified due to the absence of any externally applied current drive and the low values of β in HSX plasmas ($\beta < 0.1\%$ everywhere outside the very core, $r/a > 0.2$). Next, this VMEC equilibrium is used to calculate a database of mono-energetic transport coefficients as a function of collisionality and E_r using the DKES code to solve the drift kinetic equation [31, 32]. Finally, PENTA uses these calculated transport coefficients along with the experimentally measured temperature and density profiles to determine the particle flux as a function of E_r for each species, while restoring the conservation of momentum, which is lost in the DKES calculations. These calculated particle fluxes are then used to determine the solution for E_r which satisfies the ambipolarity constraint, where the net charge flux equals zero. Measured electron and ion temperatures near the last closed flux surface were approximately 60 and 25 eV, respectively, in all configurations for the data presented here. Electron densities were approximately $1 \times 10^{18} \text{ m}^{-3}$. Electron temperature and density profiles are measured using Thomson scattering, and ion temperatures are estimated by scaling carbon ion temperatures measured by charge exchange recombination spectroscopy in similar plasmas that had been doped with carbon.

3.2. Measurement of E_r

Using the leading pins of the Reynolds stress probe to measure floating potential, the locally measured plasma potential can be found by calculating the effect of T_e on the floating potential measurement ($V_{fl} = \Phi - \mu \frac{T_e}{T_e + T_i}$, where Φ is the plasma potential) using a procedure to estimate T_e from the fluctuating probe signals outlined in [30]. The T_e profile determined using this method matches well with the more-sparse Thomson scattering measurements in the edge. The electron temperature coefficient μ is determined by [33]

$$\mu = \ln \left(\frac{(1 - \gamma_e) A_e}{(1 + \gamma_i) A_i} \sqrt{\frac{T_e}{T_e + T_i}} \sqrt{\frac{m_i}{2\pi m_e}} \right), \quad (3)$$

where A_e/A_i is the ratio of the effective probe collection areas for electrons and ions, and γ_e and γ_i are the secondary electron emission coefficients caused by electrons and ions, respectively. Taking all of these values into account, the resulting plasma potential profile is then fitted so that the spatial derivative can be taken to calculate E_r .

The plasma potential profile in the confinement region of the QHS configuration measured by the LFS probe is given in figure 4(a). The V_{fl} measurement is taken from the moving mean of the V_{fl} signals using 1 ms time windows. The variance of this moving mean, σ_{fl}^2 , is used to propagate the errorbars and calculate the uncertainty in the final plasma potential.

The potential profile is fit to a polynomial, which is also plotted in figure 4(a) as a dashed red line, and the derivative of the fit is taken to calculate the local radial electric field. Assuming that the plasma potential Φ is constant on a flux

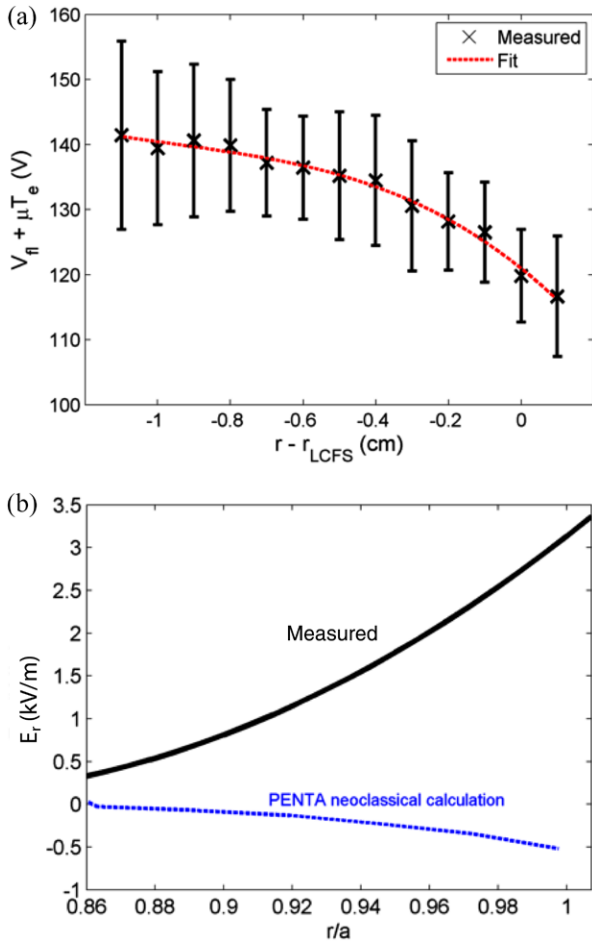


Figure 4. (a) Potential profile with a polynomial fit and (b) the resulting E_r measured by the LFS Reynolds stress probe in the QHS configuration and scaled to the flux function using equation (4), along with a comparison to neoclassical calculations from PENTA.

surface, the local radial electric field along the axis of the probe slide l is $E_{\text{probe}} = -\frac{d\Phi}{d\psi} \frac{d\psi}{dl}$. Here $\frac{d\psi}{dl}$ is the local change in magnetic flux along the axis of the probe slide, based on a translation of the probe location into VMEC flux coordinates. The measured value must be scaled by a geometric factor to find the flux function value E_r to be compared with calculated results from PENTA, which is given as $E_r = -d\Phi/dr$ where $r = \sqrt{\psi/2\pi B_0}$ is a flux function, so that

$$E_r = -\frac{d\Phi}{d\psi} \frac{d\psi}{dl} \frac{dl}{dr}, \quad (4)$$

where $\frac{d\Phi}{d\psi}$ is the radial potential gradient and the term $\frac{dl}{dr}$ is the ratio of the linear distance each probe travels to the change in radial coordinate r used by PENTA. This geometric factor is calculated to be approximately 1.7 for the LFS probe and 0.6 for the HFS probe in the QHS configuration.

The radial electric field measured in this manner using the LFS probe is plotted in figure 4(b). The values of E_r calculated by PENTA using the neoclassical ambipolarity constraint are also plotted as a blue dashed line for comparison. The measured radial electric field is significantly more positive than the

predicted neoclassical value calculated by PENTA, especially in the region where $r/a > 0.9$.

It should be noted that the non-ambipolar particle flux that is calculated for this deviation of E_r from the neoclassical solution in the QHS configuration is $<1\%$ of the total experimental particle flux in the region of interest.

3.3. Total measured $V_{||}$ profiles and comparison to neoclassical calculations in QHS

The total local ion flow in the direction of the magnetic field can be expressed as [34]

$$V_{||i} = \left(\frac{\langle V_{||i} B \rangle}{\langle B^2 \rangle} + \left(\frac{1}{enZ_i} \frac{dp_i}{d\psi} + \frac{d\Phi}{d\psi} \right) h \right) B, \quad (5)$$

where $\langle \dots \rangle$ indicates a flux surface average, $\frac{dp_i}{d\psi}$ is the ion pressure gradient, B is the local magnitude of the magnetic field, and h is a calculated geometric factor equivalent to the normalized Pfirsch–Schlüter current ($h \mathbf{B} \nabla p = \mathbf{J}_{||,PS}$) [34–36]. Positive $V_{||}$ corresponds to flow in the direction of the magnetic field, and negative is opposed. The first term in the parenthesis in equation (5) is the flux surface constant term $\frac{\langle V_{||i} B \rangle}{\langle B^2 \rangle}$, which is calculated from PENTA, and the second term is the contribution of Pfirsch–Schlüter flows.

The parallel ion velocity profile given the measured mach numbers and assumed temperature profiles is shown in figure 5. Each value plotted is the average of the moving mean of the processed signals over the final 20 ms of each discharge using a 1 ms boxcar average, and the errorbars indicate the standard deviation of the moving mean. The parallel ion flow that is calculated to result from the neoclassical ambipolar solution for E_r using equation (5) is also plotted in blue. The $\frac{\langle V_{||i} B \rangle}{\langle B^2 \rangle}$ term is calculated directly by PENTA and the local contribution from the Pfirsch–Schlüter flows at each probe for the PENTA-calculated ambipolar solution of E_r is added to the PENTA solution, which is plotted as a solid blue line. The total flow given by equation (5) calculated using the measured value of E_r is also plotted as a red dashed line.

The parallel flows measured on both the LFS and HFS probes that are depicted in figure 5 deviate significantly from the values calculated to result from the neoclassical ambipolarity condition by PENTA. The measured parallel flows are indicative of a significantly more-positive value of E_r than what is calculated using neoclassical ambipolarity (this would enter into equation (5) by increasing the flux-surface average component of the parallel flow). This result is consistent with previous experimental results in HSX which showed that the flows [37] and flow damping [38] in the direction of symmetry direction are not correctly predicted by purely neoclassical calculations. As seen in figure 5, the calculated and measured flows on the LFS are closer if the measured values of E_r are used to calculate the parallel flows. Similarly, better agreement is also seen for the Mirror and Flip-1-4 configurations, shown below in figures 7 and 9. The agreement between the calculated and measured flows is not improved on the HFS for the QHS configuration.

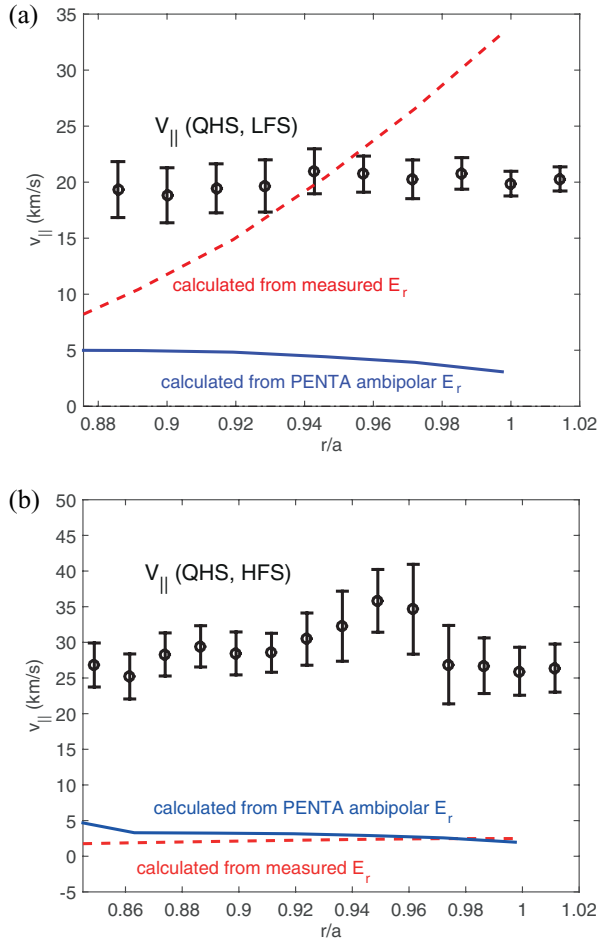


Figure 5. Parallel ion flow in the QHS configuration measured by the (a) LFS and (b) HFS mach probes. Also plotted is the total flow given by equation (5) using the calculated ambipolar solution for E_r (solid blue) and the measured E_r profile (dashed red).

3.4. E_r and V_{\parallel} measurements in configurations with symmetry degraded

The experiments presented above for the QHS configuration were repeated in similar plasma conditions in the Mirror and Flip-1-4 configurations. In the Mirror configuration, not only is the neoclassical flow damping term the largest, but the drive toward the neoclassical ambipolar solution by non-ambipolar particle fluxes is also the largest. This is because for a given deviation in the radial electric field value from the neoclassical ambipolar solution, significantly more non-ambipolar particle flux (ie, current) will be driven. The expectation for the Mirror configuration is therefore that the measured flows would be closer to the neoclassical calculations than they are in the QHS configuration.

3.4.1. E_r and V_{\parallel} measurements in the Mirror configuration. The radial electric field calculated from the locally measured potential profile using the LFS probe and scaled to the flux function value using equation (4) in the Mirror configuration is plotted in figure 6. The radial electric field deviates from the neoclassical value calculated by PENTA by as much or more in the Mirror configuration than it does in the QHS configuration (from figure 4). The parallel flow measurements in the

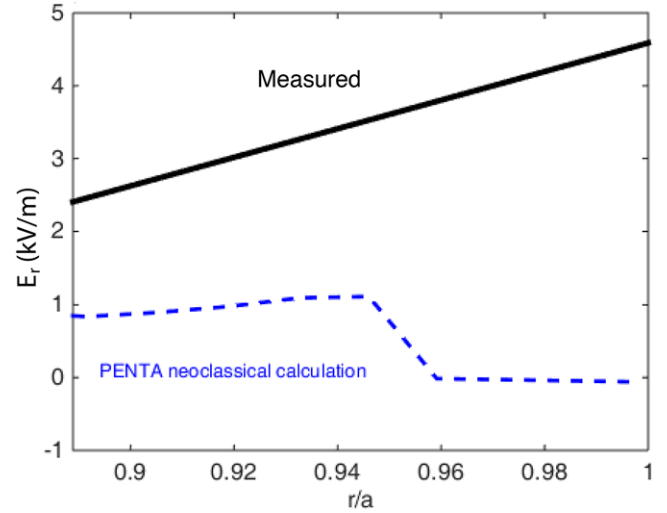


Figure 6. E_r measured by the LFS Reynolds stress probe in the Mirror configuration, and a comparison with neoclassical calculations from PENTA.

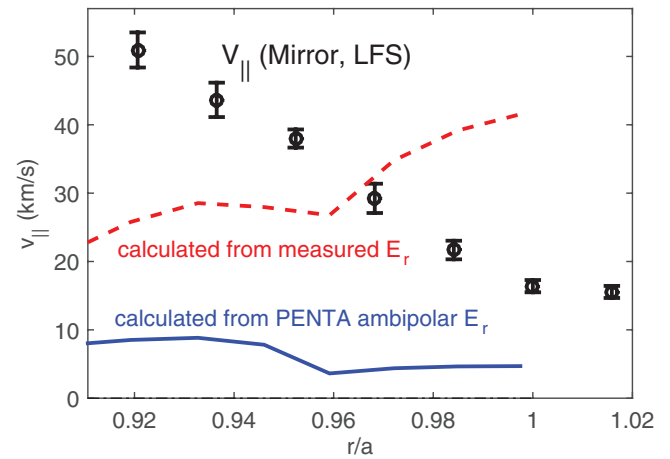


Figure 7. Parallel ion flow in the Mirror configuration measured by the LFS mach probe, compared with the total flow given by equation (5) using the calculated ambipolar solution for E_r (solid blue) and the measured E_r profile (dashed red).

Mirror configuration are then plotted in figure 7 using the LFS probe. There is a large $n = 8$, $m = 7$ island chain just outside the last closed flux surface in the Mirror configuration that may be causing additional flow damping near the boundary. The Pfirsch–Schlüter factor h from equation (5) in all configurations used here is similar to that in the QHS configuration at both probe locations, so that any changes in the parallel flows are expected to arise from a change in E_r . The calculated parallel flows using the measured values of E_r match more closely with the measured V_{\parallel} than those calculated using the ambipolar values of E_r from PENTA.

The large flows in the Mirror configuration plotted in figure 7 are a second independent measurement (along with E_r from figure 6) demonstrating that the flows deviate even more from the neoclassical ambipolar solution calculated by PENTA in the Mirror configuration than they did in the QHS configuration, especially away from the boundary island chain. One possible explanation for this is that not all electron

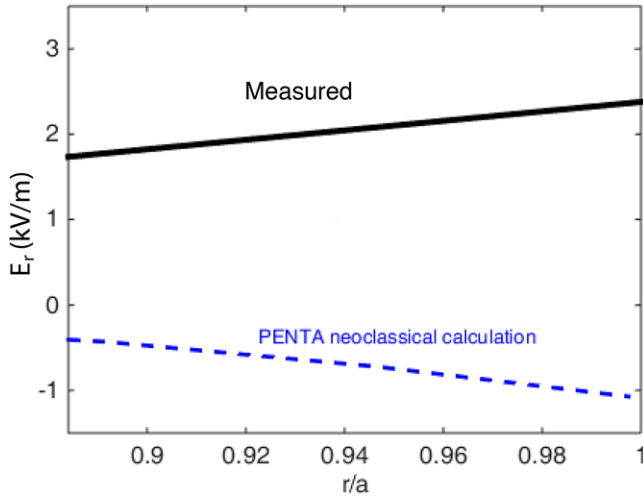


Figure 8. E_r measured by the LFS Reynolds stress probe in the Flip-1-4 configuration compared with neoclassical calculation by PENTA.

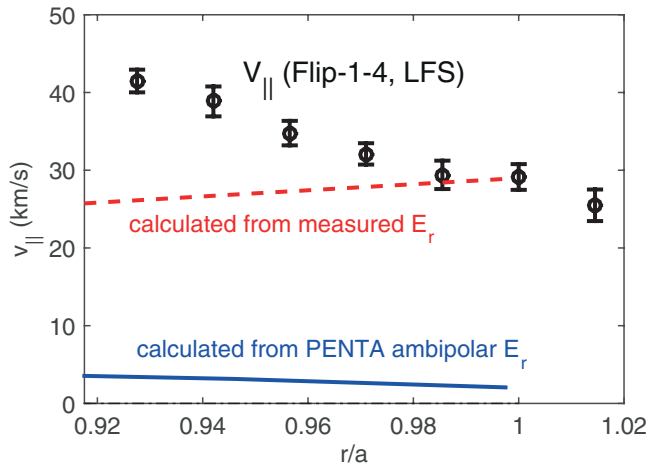


Figure 9. Parallel ion flow in the Flip-1-4 configuration measured by the LFS mach probe, compared with the total flow given by equation (5) using the calculated ambipolar solution for E_r (solid blue) and the measured E_r profile (dashed red).

losses are captured by the neoclassical transport codes, and the magnetic ripple that would lead to additional direct orbit loss or ECRH-driven electron losses is large in the Mirror configuration than in QHS. Additional ripple-trapped electron losses that are unaccounted for by DKES and PENTA would drive the ambipolar solution to a more-positive value of E_r relative to what is calculated. This hypothesis can be tested first by measuring the intrinsic flows in the Flip-1-4 configuration, which has neoclassical drive and damping terms that are between those of the QHS and Mirror configurations.

3.4.2. E_r and $V_{||}$ measurements in the Flip-1-4 configuration. The Flip-1-4 configuration has an effective ripple in the edge that is between that of the QHS and Mirror configurations. Based on the measurements of the flows in the Mirror configuration given in section 3.4.1, the collisionless loss orbits in the Mirror configuration may be driving E_r to a much larger value than what is calculated using DKES and

PENTA. By reducing the ripple compared to the Mirror configuration, measurements can be compared again with neoclassical modeling to explore the scaling of the flows with ripple.

The measured potential profile, its fit, and the resulting radial electric field using the LFS probe in the Flip-1-4 configuration are plotted in figure 8. E_r has again been scaled to the flux-function value using equation (4). The parallel flow measurements in the Flip-1-4 configuration using the LFS probe is then also plotted in figure 9. There is a small $n = 20$, $m = 18$ island at $r/a = 0.97$ at the HFS probe location that could be influencing the flows, but the island width is smaller than the radial step size of the probe scan.

The parallel flows measured are again much larger than what would be expected neoclassically based on the calculations of E_r by PENTA. Both the E_r and $V_{||}$ measurements might again be explained by additional electron particle flux that is not properly accounted for using the neoclassical transport codes.

4. Local Reynolds stress measurements

Assuming a local slab geometry, the divergence of the local Reynolds stress tensor can be written as

$$\nabla \cdot (\tilde{\mathbf{V}}\tilde{\mathbf{V}}) = \left(\hat{\rho} \frac{\partial}{\partial \rho} + \hat{b} \frac{\partial}{\partial b} + \hat{\theta} \frac{\partial}{\partial \theta} \right) \cdot (\tilde{\mathbf{V}}\tilde{\mathbf{V}}) \quad (6)$$

where $\hat{\rho} = \nabla\psi/|\nabla\psi|$ is the unit vector in the direction normal to the flux surface, \hat{b} is the unit vector in the direction of the magnetic field and $\hat{\theta}$ is the ‘bi-normal’ direction, defined here as the unit vector perpendicular to the magnetic field, but within the flux surface ($\hat{\rho} \times \hat{b} = \hat{\theta}$). These coordinates are the three orthogonal directions which are relevant for the turbulence, and they are approximately the three directions in which the Reynolds stress probes measure velocity fluctuations. The use of a slab geometry neglects additional terms due to torsion and curvature, but the terms given here are expected to be dominant given that the probe size is small relative to the local plasma shaping.

From equation (6), the terms that drive flows in the radial direction are ignored, because the flow drive within the surface is being examined rather than radial transport, and these terms are expected to be formally smaller. Next, the terms with parallel derivatives ($\frac{\partial}{\partial b} \dots$) are neglected as small compared to the other terms, because drift wave turbulence is expected to have $k_{||} \ll k_{\perp}$. Finally, because the main phenomenon being investigated and that is expected to dominate is radial momentum transport, and also because there is no measurement of the gradients in the bi-normal direction ($\frac{\partial}{\partial \theta} \dots$), these terms are neglected as well. This leaves only two terms in the expression to consider for the probe measurements,

$$\left(\nabla \cdot (\tilde{\mathbf{V}}\tilde{\mathbf{V}}) \right)_{\text{probes}} = \hat{b} \frac{\partial}{\partial \rho} (\tilde{v}_{\rho} \tilde{v}_{||}) + \hat{\theta} \frac{\partial}{\partial \rho} (\tilde{v}_{\rho} \tilde{v}_{\theta}), \quad (7)$$

where an overbar indicates a time-average. These two terms correspond to the radial transport of parallel and perpendicular

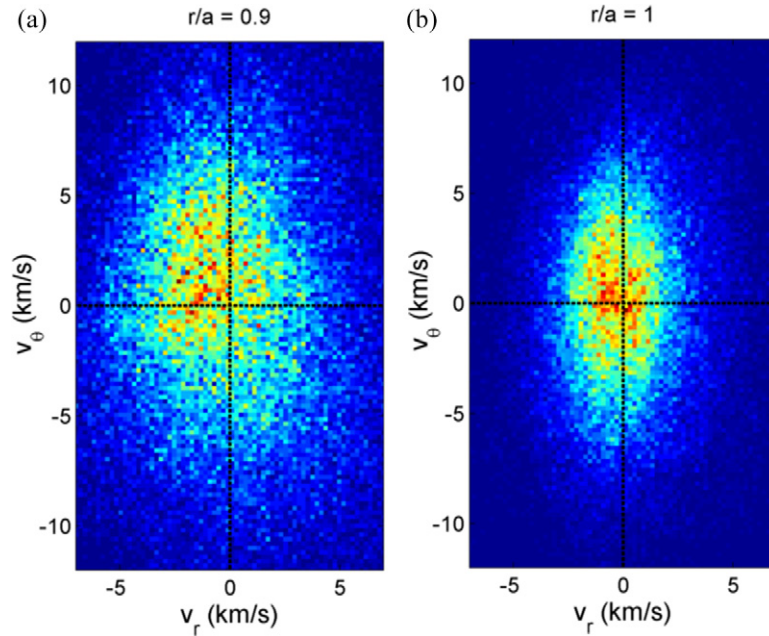


Figure 10. Probability density functions of radial and bi-normal velocity fluctuations from the LFS probe (a) inside the plasma at $r/a \approx 0.9$ and (b) near the last closed flux surface.

flow, which are each measured and included in the analysis of Reynolds stress flow drive in HSX in this work.

Measuring the local fluctuating velocity components using the setup and methodology described in section 2, the probability density function of the instantaneous radial and bi-normal velocity fluctuations as measured by the LFS probe at two different locations in a radial scan is plotted in figure 10 as a visualization of the $r - \theta$ component of the Reynolds stress. The fluctuating \tilde{v}_r and \tilde{v}_θ values are calculated for these plots for each sample time by subtracting away a moving $30 \mu\text{s}$ mean (about 3 turbulence decorrelation times). The domain is then discretized and each grid square is colored to represent how frequently the combination of \tilde{v}_r and \tilde{v}_θ fluctuations within those velocity ranges coincided with each other, with red being the most frequent and blue being the least frequent.

Near the last closed flux surface, where the data from figure 10(b) was taken, the fluctuations are mostly isotropic. Positive radial fluctuations correlate roughly equivalently with both positive and negative bi-normal velocity fluctuations, and likewise for negative radial fluctuations. Further inside the plasma, where the data from figure 10(a) was taken, positive \tilde{v}_r fluctuations correlate more frequently with negative \tilde{v}_θ fluctuations and vice-versa. The integrated result of this skewed PDF is a negative value of the time-averaged Reynolds stress term $\overline{\tilde{v}_r \tilde{v}_\theta}$.

The fluctuations depicted in figure 10 could also be considered a visualization of the local tilt of the turbulent eddies. If these locally measured fluctuations were indicative of a flux surface average value of the Reynolds stress in the bi-normal direction, then the change in Reynolds stress across the minor radius demonstrated by the fluctuation PDFs in figure 10 would imply a flow drive in the bi-normal direction according to equation (7), since the Reynolds stress torque

in this direction is proportional to the radial gradient of $\overline{\tilde{v}_r \tilde{v}_\theta}$. Previous experiments using multiple instances of Langmuir probes have found that there is no evidence of long-range correlations or bicoherence of poloidal electric field fluctuations in similar unbiased plasmas in the edge of HSX in either the QHS or the Flip-1-4 configurations [39], suggesting that these are not short radial wavelength zonal flows.

For the work here, the fluctuating component of the term $\nabla \cdot (m n \mathbf{V} \mathbf{V})$ in the momentum balance equation is approximated using only the part given in equation (6), $m n \nabla \cdot (\tilde{\mathbf{V}} \tilde{\mathbf{V}})$. This assumes that the density fluctuations may be neglected, which is valid as these terms are measured using the probes to be at least an order of magnitude smaller than the velocity fluctuation terms in most cases ($\mathbf{V} \tilde{n} \tilde{\mathbf{V}} \ll n \tilde{\mathbf{V}} \tilde{\mathbf{V}}$). The density and velocity fluctuations are not correlated with each other in the same way that the radial and poloidal velocity components are in figure 10(a).

4.1. Reynolds stress profiles in the QHS configuration

In order to calculate the local Reynolds stress based on the measured fluctuating quantities, the final 20 ms of data from each 50 ms discharge was discretized into $50 \mu\text{s}$ time windows for mean subtraction. The average Reynolds stress in these time windows is then the quantity shown. To estimate the contribution to the momentum that would result from this measured Reynolds stress, a gradient must then be calculated from the measured shot-by-shot profile, because the Reynolds stress drive term is proportional to the radial gradient of $\overline{\tilde{v}_r \tilde{v}_\theta}$, as shown in equation (7). The measured points are fit to a curve, and the derivative of the curve is taken to estimate the time-averaged Reynolds stress force. In the cases presented here, a second order polynomial fit was found to agree sufficiently well with the data.

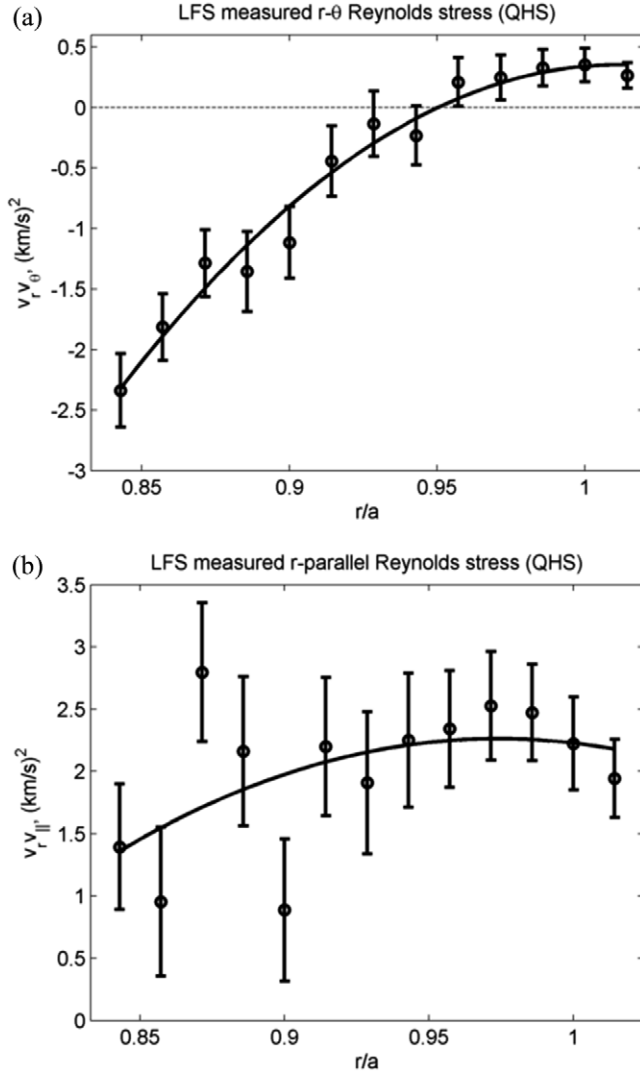


Figure 11. Radial profiles of (a) $\overline{v_r v_\theta}$ and (b) $\overline{v_r v_\parallel}$ measured by the LFS probe in the QHS configuration, along with polynomial fits.

The measured Reynolds stress profiles using the LFS probe in the QHS configuration are plotted in figure 11 along with the fitted curves. The bi-normal component of the Reynolds stress, $\overline{v_r v_\theta}$, is plotted in figure 11(a), and the parallel component, $\overline{v_r v_\parallel}$, is plotted in figure 11(b). The radial gradient of $\overline{v_r v_\theta}$ provides a drive for rotation in the $\hat{\theta}$ direction, and the radial gradient of $\overline{v_r v_\parallel}$ provides a drive for rotation in the parallel direction. Both of these terms are important for determining the rotation and E_r , if indeed the Reynolds stress is the dominant factor in its determination. The errorbars indicate the standard deviation of the discrete time windows used in the ensemble for each discharge.

Although there is a gradient to the fitted curve of the parallel Reynolds stress in figure 11(b), the gradient is small relative to the statistical uncertainty and radial variability of the measurement. This is in contrast to the bi-normal Reynolds stress in figure 11(a), which shows a clear, consistent radial gradient across the region spanned by the probe.

The Reynolds stress profiles measured by the HFS probe are then plotted in figure 12(a) for the bi-normal component and figure 12(b) for the parallel component.

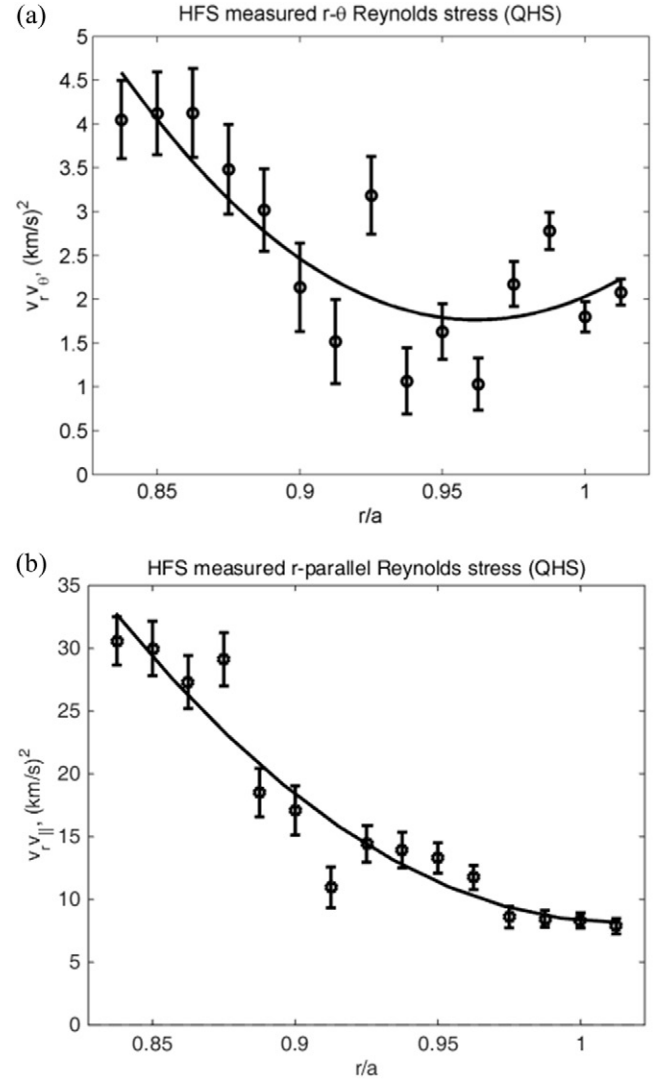


Figure 12. Radial profiles of (a) $\overline{v_r v_\theta}$ and (b) $\overline{v_r v_\parallel}$ measured by the HFS probe in the QHS configuration, along with polynomial fits.

The differences between the measurements made using the LFS and HFS probes are significant enough that a general statement cannot be made regarding the flux surface average of the Reynolds stress based on the measurements at these two discrete locations. The existence of stellarator symmetry in all of the configurations presented here would be expected to cause the Reynolds stress from each half field period to negate that of every neighboring half field period, resulting in a near-zero flux surface averaged Reynolds stress. Given the magnitude of these measured fluctuations, however, small deviations in stellarator symmetry could result in macroscopically meaningful levels of Reynolds stress torque.

4.2. Momentum evolution and steady state solution

To estimate the rotation that would result from the measured Reynolds stress, the inferred torque from the measured Reynolds stress profile is extrapolated to a flux surface average and balanced against a calculated viscosity. Assuming that neoclassical viscosity and ion-neutral friction are the dominant

damping mechanisms that are balancing the Reynolds stress as the dominant drive term, the flow evolution equations can be written in the form of a pair of coupled differential equations as [17]

$$\frac{\partial \langle \mathbf{B} \cdot \mathbf{V} \rangle}{\partial t} = -\frac{1}{n_i m_i} \langle \mathbf{B} \cdot \nabla \cdot \Pi \rangle - \nu_{in} \langle \mathbf{B} \cdot \mathbf{V} \rangle - B_0 \left\langle \frac{\partial}{\partial \rho} (\bar{v}_\rho \bar{v}_\parallel) \right\rangle, \quad (8)$$

$$\frac{\partial \langle \mathbf{B}_p \cdot \mathbf{V} \rangle}{\partial t} = -\frac{1}{n_i m_i} \langle \mathbf{B}_p \cdot \nabla \cdot \Pi \rangle - \nu_{in} \langle \mathbf{B}_p \cdot \mathbf{V} \rangle - B_p \left\langle \frac{\partial}{\partial \rho} (\bar{v}_\rho \bar{v}_\theta) \right\rangle, \quad (9)$$

where \mathbf{B}_p is the poloidal component of the main field, $\rho = \frac{\nabla \psi}{|\nabla \psi|}$ is the radial coordinate, ν_{in} is the damping rate due to ion-neutral collisions and $\langle \dots \rangle$ indicates a flux surface average. The Reynolds stress terms are also taken as a time-average. Here ν_{in} will be calculated as [40]

$$\nu_{in} \approx N_n 10^{-14} T_i^{0.318}, \quad (10)$$

where N_n is the neutral particle density in m^{-3} . The bi-normal fluctuating velocity component v_θ has been approximated to be in the poloidal direction for these calculations. The neoclassical parallel and poloidal viscosity can be calculated analytically for ions in the plateau collisionality regime as [41, 42]

$$\langle \mathbf{B} \cdot \nabla \cdot \Pi \rangle = (n_i m_i B_0) v_{ti} \frac{\sqrt{\pi}}{2} [(\iota \alpha_P + \alpha_C) U^\alpha + (\iota \alpha_C + \alpha_T) U^\zeta], \quad (11)$$

$$\langle \mathbf{B}_p \cdot \nabla \cdot \Pi \rangle = (n_i m_i B_p) v_{ti} \frac{\sqrt{\pi}}{2} \iota (\alpha_P U^\alpha + \alpha_C U^\zeta), \quad (12)$$

where ι is the rotational transform, v_{ti} is the ion thermal velocity, U^α and U^ζ are the flows in the Hamada poloidal and toroidal directions, respectively, $\alpha_T = \sum n^2 b_{n,m}^2 / |n - m|$, $\alpha_P = \sum m^2 b_{n,m}^2 / |n - m|$, $\alpha_C = -\sum n m b_{n,m}^2 / |n - m|$, and each of the sums are taken over all spectral components $b_{n,m}$ in the configuration. In the QHS configuration, the $n = 4, m = 1$ mode dominates the neoclassical damping, but the total evolution time of the flows in the edge region is dominated by the neutral viscosity. This result, that the analytically calculated damping in the quasi-symmetric direction is dominated by the neutral viscosity, was previously reported for 0.5 T plasmas in HSX [38]. The neutral density profiles are calculated using the DEGAS Monte Carlo neutral gas modeling code using measurements from an array of H-alpha detectors and Thomson scattering.

Given the fit to the $r - \theta$ Reynolds stress measurements from figure 11(a), the bi-normal Reynolds stress drive is inserted into equation (9) and the coupled flows are evolved by integrating the equations until they reach steady state. The resulting time-dependent flows are presented in figure 13, starting from a zero-velocity initial condition. The parallel component of the Reynolds stress has been neglected for this example calculation. All values used in the calculations plotted here were taken from a radial location of $r/a = 0.9$.

As demonstrated in figure 13, the magnitude of the parallel flows that are calculated to result from the measured Reynolds stress are many times larger than the experimentally measured

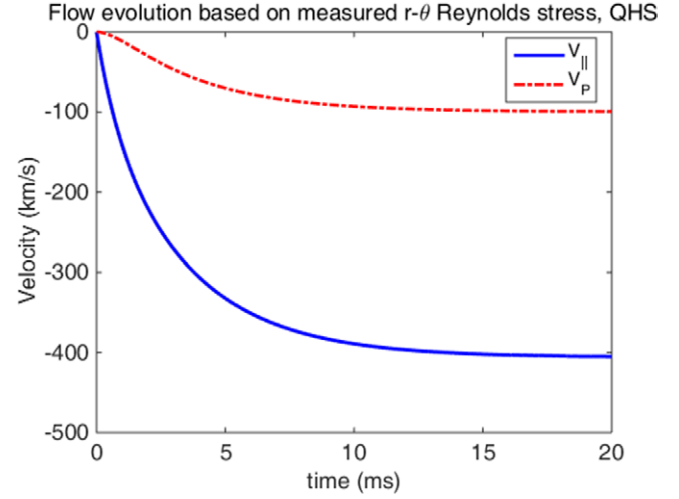


Figure 13. Momentum evolution from equation (9) in the QHS configuration near $r/a = 0.9$ resulting from the bi-normal component of the Reynolds stress measured by the LFS probe.

values in the QHS configuration from section 3.3, and the direction is opposite of the measured flow. It should be noted again, however, that the Reynolds stress should be taken as a flux surface averaged value, where here it has been measured locally and the local measurement is assumed to be indicative of a flux surface average for the purposes of evaluating the magnitude of the drive. For the rest of this work, only the final steady-state velocities will be used, since all of the data analyzed here is from experiments in steady state plasmas.

This method is similar to the one utilized in the linear device CSDX to calculate a rotation profile that matched the measured rotation in the azimuthal direction [12, 13]. Calculating the viscosity in HSX is much more complicated than in a collisional linear device, however, and previous experiments have demonstrated that the experimental viscosity in HSX is several times larger than what is calculated by the analytic method used here [17].

Assuming for the moment that the local Reynolds stress measured using each probe independently is indicative of a flux surface average, the resulting saturated parallel velocities calculated by the momentum evolution using equation (9) is given in figure 14. Both the parallel and bi-normal components of the Reynolds stress are included in this calculation.

Figure 14 shows that the Reynolds stress profiles measured at the LFS and HFS probe locations both lead to large flow drive terms, and that they actually drive the total flow in opposite directions. Although only the parallel component of the flow is shown, the total calculated flow in each case follows the helical direction of symmetry.

In order for the momentum evolution from equation (9) to saturate at flow values that are similar to those observed experimentally near the last closed flux surface ($V_\parallel \approx 20 \text{ km s}^{-1}$ based on measurements from section 3.3), the flux surface averaged gradient of the bi-normal Reynolds stress would need to be $\approx 0.1 (\text{km s}^{-1})^2 \text{ m}^{-1}$. This is about a factor of 20 smaller than the average gradient across the edge region using the LFS probe. Due to the fact that the neutral viscosity dominates the modeled damping in the direction of symmetry in

the QHS configuration and that the neutral density gradient is large in the edge, the necessary Reynolds stress that is calculated to drive the flows would decrease rapidly further inside the plasma, as well.

Given the difference between the derived flow drive from the two probe locations, as well as the difference in magnitude between the measured equilibrium flows and the extrapolated Reynolds stress drives, it is clear based on these measurements that the flux surface averaged Reynolds stress cannot be extracted from two locations on a flux surface alone. More information about the variation of Reynolds stress on a flux surface is required to fully account for the Reynolds stress in the equilibrium momentum balance. The variation of turbulence on a flux surface and its dependence on magnetic geometry has previously been explored in the TJ-K stellarator [43], but a similar study in HSX would require the installation of a comparable probe array.

5. Contribution of Reynolds stress to flows in different configurations

In section 3.4, it was shown that E_r and $V_{||}$ in the Mirror and Flip-1-4 configurations deviated more from the neoclassically calculated solutions for the flows than they did in the QHS configuration. This result is in contradiction to expectations that plasmas in these configurations would be driven more strongly toward the neoclassical solutions. One reason for this observation could be that the Reynolds stress is larger in these configurations than it is in the QHS configuration, but this section presents measurements showing that this is not the case.

As shown by the differences between the measurements of the Reynolds stress made using the LFS and HFS probes in figures 11 and 12, it is not appropriate to extrapolate two local measurements of the Reynolds stress to a flux surface average. To estimate how the Reynolds stress scales with measured fluctuating quantities, the Diamond and Kim scaling of the Reynolds stress drive is used here, which gives [44]

$$J_r \approx n_0 e c_s \left(\frac{e\tilde{\phi}}{T_e} \right)^2 k_\theta \rho_s, \quad (13)$$

where $c_s = \sqrt{(T_e + T_i)/m_i}$ is the sound speed, $\rho_s = c_s/\Omega_i$ is the sound speed over the ion gyroradius, and k_θ is the wave-number in the bi-normal direction.

Although it contains no cross-phase information, the scaling from equation (13) finds that the Reynolds stress drive is expected to scale approximately with the fluctuating potential squared. If adiabatic electrons are assumed so that $\frac{e\tilde{\phi}}{T_e} \approx \frac{\tilde{n}}{n}$, then the normalized density fluctuations can be estimated from the ion saturation current measurements. Using $I_{\text{sat}} = 0.6n_i e A_i \sqrt{\frac{T_e}{m_i}}$ [45] and assuming quasi-neutrality and that electron temperature fluctuations are negligible, the measurement can be related directly to the fluctuating density so that $\frac{\tilde{n}}{n} \approx \frac{\tilde{I}_{\text{sat}}}{I_{\text{sat}}}$. Using this approximation, the normalized density fluctuations as measured by the LFS probe in the QHS,

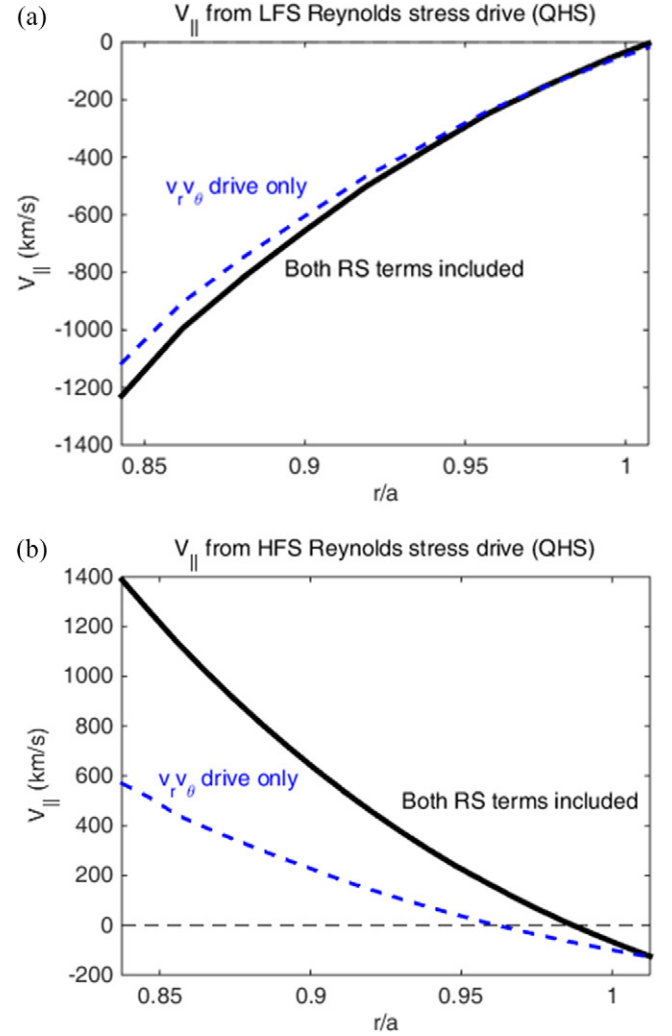


Figure 14. Parallel flow inferred from the saturated evolution of equation (9) in the QHS configuration using both the parallel and bi-normal components of the Reynolds stress drive measured by the (a) LFS and (b) HFS probes.

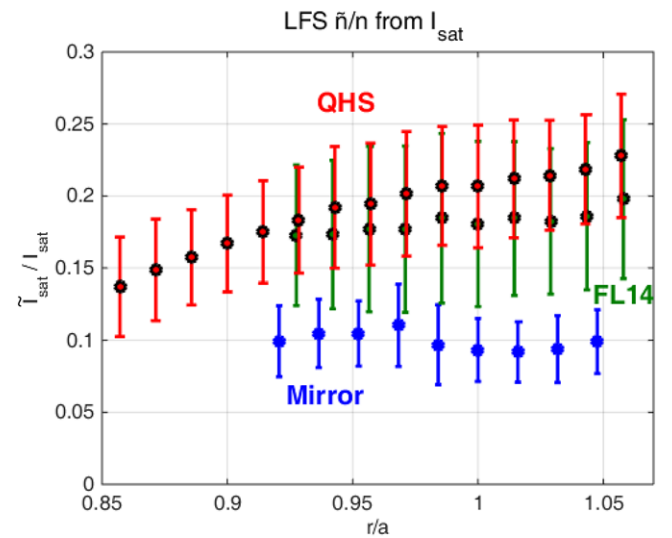


Figure 15. Normalized density fluctuation profiles, $\tilde{I}_{\text{sat}}/I_{\text{sat}}$, in the QHS, Flip-1-4 and Mirror configurations.

Flip-1-4 and Mirror configurations are plotted in figure 15. The I_{sat} measurements from each side of the insulating barrier of the mach probe are added together for the total I_{sat} signal in this analysis. Filtering of high frequency noise in the I_{sat} signals reduced the magnitude of the fluctuation amplitudes presented here slightly, but did not alter the qualitative results.

In the Mirror configuration, the normalized magnitude of the density fluctuations is about half as large as they are in the QHS configuration in the radial region measured by the probes. Fluctuations in the Flip-1-4 configuration are also reduced slightly relative to the QHS configuration. The launched power was the same in all configurations here, but the absorbed power was less in the Mirror and Flip-1-4 cases than in the QHS configuration, so that the total heat flux through the last closed flux surface is reduced in these cases. This may explain the result of reduced fluctuations in the Mirror and Flip-1-4 configuration, which had reduced heat flux through the edge.

Combining these measurements with the simple estimate of the scaling from figure 15, the Reynolds stress drive would be expected to be about 4 times larger in the QHS case than in the Mirror configuration. Based on the scaling from equation (13) and the normalized fluctuations plotted in figure 15, the Reynolds stress may still be a large and important term in the momentum balance in these configurations, but it is generally smaller than it is in the QHS configuration. The Reynolds stress therefore does not appear to account for the increase in flows observed in the Mirror and Flip-1-4 configurations relative to QHS.

Including the cross-phase information of the locally measured Reynolds stress in the Mirror and Flip-1-4 configurations does not qualitatively change this result [30]. When the predicted saturated flows are calculated and compared to those for the QHS configuration from figure 14, the magnitudes of the resulting flows are not significantly larger than the QHS case, and the problem remains that the measurements at two points on a flux surface differ qualitatively from each other and cannot be reliably extrapolated to a flux surface average.

An alternative explanation for the mismatch between calculated and measured flows is that ECRH-driven flux needs to be accounted for in the neoclassical modeling, which is left for future work. Some additional electron flux would qualitatively bring the PENTA modeling into better agreement with the flow measurements. Previous studies in HSX have found that rotation in the symmetry direction increases when the ECRH power is increased, in both the QHS and Flip-1-4 configurations [23]. Injecting additional ECRH power lead to a large fast electron population which interfered with the probe measurements, so only low-power, high density discharges were available for this study.

6. Discussion

Using Langmuir probes, the measured radial electric field and parallel ion flow in the edge of the QHS configuration of HSX deviate from the purely neoclassical values that are calculated using PENTA. The locally measured Reynolds

stress gradient on the high and low field sides is large and is of opposite sign for the two locations. Therefore, a full flux surface average of the Reynolds stress cannot be extrapolated from the locally observed fluctuations. However, it is still possible that Reynolds stress influences the plasma rotation in the QHS configuration, but additional modeling is necessary. Measurements in configurations with the quasi-symmetry degraded are found to have larger flows which deviate from the neoclassically calculated flows even more than they did in the QHS configuration. At the same time, the fluctuation amplitudes for these configurations decrease. This suggests that Reynolds stress is not responsible for the additional rotation, although it may still play a role in each case.

The radial electric field in the edge, as measured directly and inferred from parallel flow measurements, is found to be more positive than what is predicted by neoclassical transport codes. A similar result has been observed previously in the edge of the LHD [46]. In the LHD case, the measurements of radial electric field matched more closely with modeling further inside of the device, but the deviation at the edge was large. This could be an indication that additional physics such as ECRH-driven particle losses or direct loss orbits of collisionless trapped electrons may need to be included in the modeling to correctly predict E_r using the neoclassical ambipolarity constraint. Consistent with this hypothesis, the measurements show that the parallel flow becomes more positive with the effective ripple.

The results presented here suggest the value of performing nonlinear gyrokinetic calculations to understand whether Reynolds stress makes a significant contribution to momentum balance at the edge of a quasisymmetric stellarator. Such a calculation would make it possible to actually determine the flux surface average of the drive. In particular, it would then be possible to compare the results of the simulations to measurements made at two locations in the torus.

Acknowledgments

The authors would like to thank L Stephey, C Deng, K Likin, S Kumar and M Frankowski for their assistance over the course of this work. This work is supported by US DOE Grant DE-FG02-93ER54222. Data relevant to all figures and tables is available for access from the HSX website at www.hsx.wisc.edu/HSX_Publication_Data.shtml.

References

- [1] Rutherford P.H. 1970 *Phys. Fluids* **13** 482
- [2] Hinton F.L. and Hazeltine R.D. 1976 *Rev. Mod. Phys.* **48** 239
- [3] Hirshman S.P. 1978 *Nucl. Fusion* **18** 917
- [4] Boozer A.H. 1983 *Phys. Fluids* **26** 496
- [5] Helander P. and Simakov A. 2008 *Phys. Rev. Lett.* **101** 145003
- [6] Parra F.I. and Catto P.J. 2010 *Plasma Phys. Control. Fusion* **52** 059801
- [7] Parra F.I., Barnes M. and Catto P.J. 2011 *Nucl. Fusion* **51** 113001
- [8] Calvo I. and Parra F.I. 2012 *Plasma Phys. Control. Fusion* **54** 115007

- [9] Rice J.E. et al 2007 *Nucl. Fusion* **47** 1618–24
- [10] Helander P. and Simakov A.N. 2010 *Contrib. Plasma Phys.* **50** 695–700
- [11] Calvo I., Parra F.I., Velasco J.L. and Alonso J.A. 2013 *Plasma Phys. Control. Fusion* **55** 125014
- [12] Holland C., Yu J., James A., Nishijima D., Shimada M., Taheri N. and Tynan G. 2006 *Phys. Rev. Lett.* **96** 195002
- [13] Tynan G.R., Holland C., Yu J.H., James A., Nishijima D., Shimada M. and Taheri N. 2006 *Plasma Phys. Control. Fusion* **48** S51–73
- [14] Müller S.H., Boedo J.A., Burrell K.H., deGrassie J.S., Moyer R.A., Rudakov D.L. and Solomon W.M. 2011 *Phys. Rev. Lett.* **106** 115001
- [15] Solomon W.M., Burrell K.H., deGrassie J.S., Boedo J., Garofalo A., Moyer R., Muller S., Petty C. and Reimerdes H. 2011 *Nucl. Fusion* **51** 073010
- [16] Anderson F.S.B., Almagri A.F., Anderson D.T., Matthews P., Talmadge J.N. and Shohet J.L. 1995 *Fusion Technol.* **27** 273
- [17] Gerhardt S.P., Talmadge J.N., Canik J.M. and Anderson D.T. 2005 *Phys. Plasmas* **12** 056116
- [18] Canik J.M., Anderson D.T., Anderson F.S.B., Clark C., Likin K.M., Talmadge J.N. and Zhai K. 2007 *Phys. Plasmas* **14** 056107
- [19] Nemov V.V., Kasilov S.V., Kernbichler W. and Heyn M.F. 1999 *Phys. Plasmas* **6** 4622
- [20] Guttenfelder W., Anderson D.T., Anderson F.S.B., Canik J.M., Likin K.M. and Talmadge J.N. 2009 *Phys. Plasmas* **16** 082508
- [21] Guttenfelder W., Lore J., Anderson D.T., Anderson F., Canik J., Dorland W., Likin K. and Talmadge J. 2008 *Phys. Rev. Lett.* **101** 215002
- [22] Lore J. 2010 *Dissertation*, University of Wisconsin, Madison
- [23] Briesemeister A. 2013 *Dissertation*, University of Wisconsin, Madison
- [24] Gennrich F.P. and Kendl A. 2012 *Plasma Phys. Control. Fusion* **54** 015012
- [25] Hutchinson I.H. 2002 *Plasma Phys. Control. Fusion* **44** 1953
- [26] Hirshman S.P., Van Rij W.I. and Merkel P. 1986 *Comput. Phys. Commun.* **43** 143–55
- [27] Weir G.M., Faber B.J., Likin K.M., Talmadge J.N., Anderson D.T. and Anderson F.S.B. 2015 *Phys. Plasmas* **22** 056107
- [28] Lore J., Guttenfelder W., Briesemeister A., Anderson D.T., Anderson F.S.B., Deng C.B., Likin K.M., Spong D.A., Talmadge J.N. and Zhai K. 2010 *Phys. Plasmas* **17** 056101
- [29] Spong D.A. 2005 *Phys. Plasmas* **12** 056114
- [30] Wilcox R.S. 2014 *Dissertation*, University of Wisconsin, Madison
- [31] Hirshman S.P., Shaing K.C., van Rij W.I., Beasley C.O. and Crume E.C. 1986 *Phys. Fluids* **29** 2951
- [32] van Rij W.I. and Hirshman S.P. 1989 *Phys. Fluids B* **1** 563
- [33] Schrittwieser R. et al 2002 *Plasma Phys. Control. Fusion* **44** 567
- [34] Coronado M. and Talmadge J.N. 1993 *Phys. Fluids B* **5** 1200
- [35] Nemov V.V. 1988 *Nucl. Fusion* **28** 1727
- [36] Coronado M. and Wobig H. 1992 *Phys. Fluids B* **4** 1294
- [37] Briesemeister A., Zhai K., Anderson D.T., Anderson F.S.B. and Talmadge J.N. 2013 *Plasma Phys. Control. Fusion* **55** 014002
- [38] Gerhardt S., Talmadge J.N., Canik J. and Anderson D.T. 2005 *Phys. Rev. Lett.* **94** 015002
- [39] Wilcox R.S., van Milligen B.P., Hidalgo C., Anderson D.T., Anderson F.S.B. and Ramisch M. 2011 *Nucl. Fusion* **51** 083048
- [40] Cornelis J., Sporken R., Oost G. and Weynants R. 1994 *Nucl. Fusion* **34** 171
- [41] Coronado M. and Wobig H. 1986 *Phys. Fluids* **29** 527
- [42] Shaing K.C., Hirshman S.P. and Callen J.D. 1986 *Phys. Fluids* **29** 521
- [43] Birkenmeier G., Ramisch M., Manz P., Nold B. and Stroth U. 2011 *Phys. Rev. Lett.* **107** 025001
- [44] Diamond P.H. and Kim Y. 1991 *Phys. Fluids B* **3** 1626
- [45] Hershkovitz N. 1989 *Plasma Diagnostics* (Amsterdam: Elsevier) p 113
- [46] Matsuoka S., Satake S., Yokoyama M. and Wakasa A. 2011 *Plasma Fusion Res.* **6** 1203016